

## The Breakdown of a 316L Stainless Steel Oxide Film in an AlCl<sub>3</sub>-EMIC Ionic Liquid

Jiani Huang, Zhehang Pan, Lun Jiang, and Guoping Ling\*

School of Materials Science and Engineering, Zhejiang University, Hangzhou 310027, China

\*E-mail: [linggp@zju.edu.cn](mailto:linggp@zju.edu.cn)

Received: 10 February 2019 / Accepted: 20 April 2019 / Published: 10 June 2019

---

The breakdown of the oxide film on 316L stainless steel was investigated in an acidic aluminum chloride-1-ethyl-3-methylimidazolium chloride (AlCl<sub>3</sub>-EMIC) ionic liquid by linear sweep voltammetry, chronoamperometry and the pulse potentiostatic method. Scanning electron microscopy and atomic force microscopy were used to characterize the surface morphology. The results showed that the breakdown of the oxide film depended on the anodic dissolution potential, and the general breakdown occurred when the potential exceeded a critical potential. The general breakdown occurred instantaneously at a large number of positions all over the surface and was followed by a planar dissolution pattern. The oxide film remained on the surface after the general breakdown unless it was removed by stirring. The mechanism of the general breakdown of the oxide film and the subsequent planar dissolution pattern are discussed.

---

**Keywords:** Oxide film; General breakdown; Ionic liquid; Stainless steel; Electrochemical etching

### 1. INTRODUCTION

Oxide films are commonly found on metal surfaces. The removal of the oxide film is necessary for many metal surface treatment methods, such as electroplating, electroless plating, ion plating, spraying, chemical vapor deposition, and physical vapor deposition, to improve the adhesion between the coating and substrate [1]. Traditionally, mechanical polishing and acid pickling were used to remove the oxide film. However, after the removal of the native oxide film, a new oxide film would rapidly reform on reactive metals and their alloys, such as aluminum, magnesium, titanium, and stainless steel, due to their high affinity for oxygen and water, leading to bad adhesion [1-3].

Recently, a method of anodic dissolution in ionic liquids (ILs) has been proposed to remove the oxide film on the metal surface [4-6]. ILs contain ions with a melting point below 100 °C and possess attractive properties, such as a wide electrochemical window, low vapor pressure and high thermal stability [7, 8]. When a fresh metal surface is protected by non-aqueous ILs and an inert atmosphere

provided by a glove box after anodic dissolution, it barely reoxidizes.

There are two patterns of anodic dissolution of metal in ILs: local dissolution and general dissolution, which correspond to the incomplete and complete removal of the oxide film, respectively [9, 10]. Many studies have shown that the pattern of anodic dissolution is influenced by several factors, such as the ion species in the IL [11, 12], anode materials [13], and electrochemical parameters [9, 10, 14]. Furthermore, some studies indicated that mechanical polishing in a protective environment can lead to local dissolution, and the authors explained that the native oxide film was broken locally by mechanical polishing and that the anodic dissolution of the metal occurred preferentially at these locations [15, 16].

Stainless steel is widely used in the chemical industry, energy industry and other fields. Due to the high affinity of stainless steel to oxygen, a dense oxide film always forms on its surface. In chloride-containing acidic  $\text{AlCl}_3$ -EMIC IL, we found general dissolution on a 316L stainless steel [17], which was supposed to be related to the general breakdown of the oxide film on the surface. However, in a chloride-containing aqueous solution, the local dissolution in the form of pitting typically occurs on 316L stainless steel when dissolving anodically, and the reason for local dissolution was related to local breakdown of oxide film [18-29]. It is difficult to explain the general breakdown of the oxide film in the chloride-containing IL with the current local breakdown mechanism. In this paper, we studied the breakdown of oxide film in an acidic  $\text{AlCl}_3$ -EMIC IL on mirror finished 316L stainless steel, and the breakdown mechanism is discussed.

## 2. EXPERIMENTAL

Aluminum chloride ( $\text{AlCl}_3$ , anhydrous powder, Sinopharm Chemical Reagent Co., Ltd. > 99.0%) was used as received and 1-ethyl-3-methylimidazolium chloride (EMIC) was prepared according to a previous paper [30]. An acidic  $\text{AlCl}_3$ -EMIC ionic liquid was prepared by mixing the two components (2:1 molar ratio  $\text{AlCl}_3$  to EMIC) and then stirring continuously for 24 hours. All experiments involving ionic liquid were handled under a purified argon atmosphere in a glove box, where the moisture and oxygen content were maintained below 1 ppm.

A three-electrode electrochemical cell was used in the electrochemical experiment. A mirror finished SUS 316L stainless steel plate (Shanghai Yoogle Metal Technology Co., Ltd.) was used as the working electrode. The average roughness  $R_a$  of the 316L stainless steel was approximately 10 nm, measured by a roughness measuring instrument at a length of 5 mm, and the chemical composition is shown in Table 1. The thickness of the oxide film examined by X-ray photoelectron spectroscopy and ellipsometry (not shown in the article) was approximately 3 nm. The working electrode was ultrasonically cleaned in ethanol for 10 min and then sealed to leave an exposed surface area of 1  $\text{cm}^2$ . An Al plate (99.999%) was used as the counter electrode, and an Al wire placed in a glass tube containing 2:1  $\text{AlCl}_3$ -EMIC IL with a porous ceramic frit at the bottom was used as the reference electrode.

**Table 1.** Chemical composition of SUS 316L stainless steel in wt.%

Elements	C	Si	Mn	P	S	Ni	Cr	Mo
Content	0.017	0.548	1.346	0.0349	0.0031	10.03	16.54	2.07

Electrochemical measurements performed at room temperature were carried out using a Princeton Parstat 2273 electrochemical workstation and PowerSuite software. A scan rate of  $10 \text{ mV s}^{-1}$  was used in linear sweep voltammetry (LSV) experiments, and the data were collected every  $0.1 \text{ s}$  for the chronoamperometry and pulse potentiostatic experiments. The uncompensated solution resistance was determined by electrochemical impedance spectroscopy (EIS), and approximately 90% of the  $iR$  drop was compensated in the LSV experiments and potentiostatic experiments.

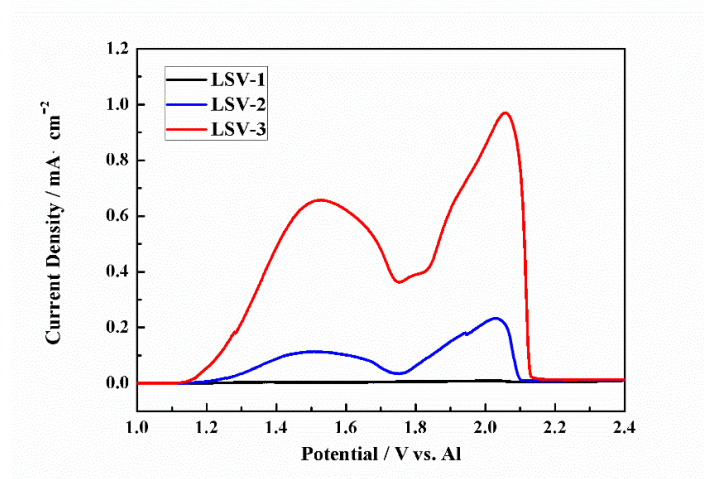
Surface analysis was carried out using scanning electron microscopy (SEM, Hitachi SU-70). Atomic force microscopy (AFM, Cypher S) measurements were conducted using microfabricated Si cantilevers with a force constant of approximately  $40 \text{ N m}^{-1}$ .

### 3. RESULTS

#### 3.1. Linear sweep voltammetry

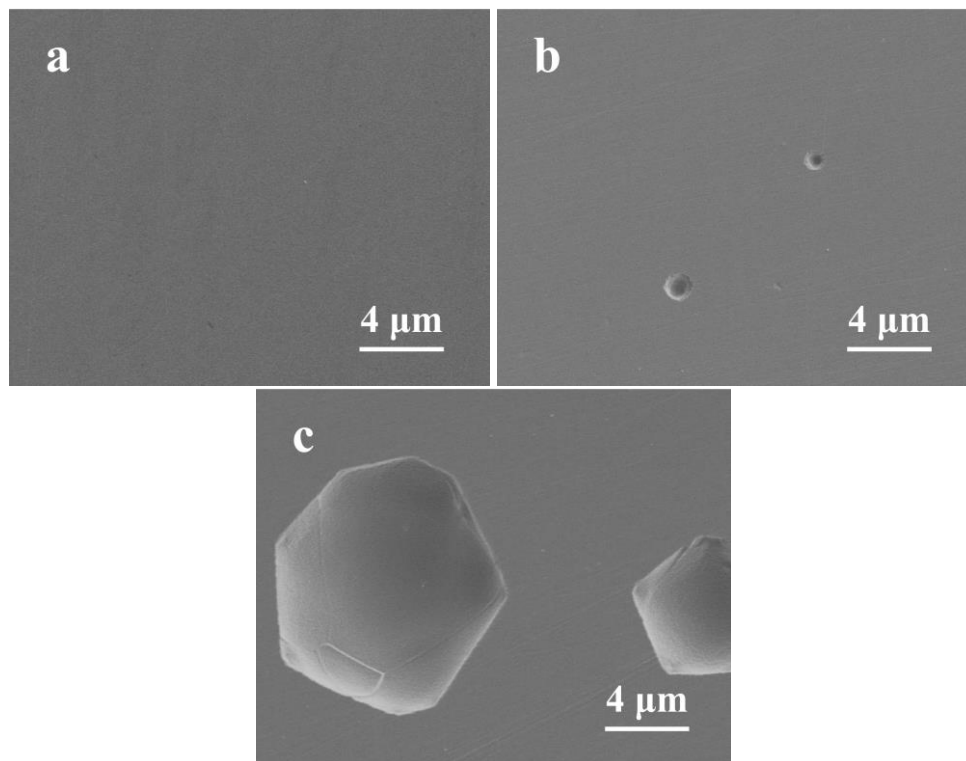
To explore the anodic dissolution behavior of 316L stainless steel in a 2:1  $\text{AlCl}_3$ -EMIC ionic liquid, linear sweep voltammetry experiments were carried out within the potential range from the open-circuit potential (OCP,  $0.9 \text{ V}$ ) to  $2.4 \text{ V}$  and  $5.0 \text{ V}$  vs. Al.

Fig. 1 shows linear sweep voltammetry curves within the potential range from OCP to  $2.4 \text{ V}$ . The anodic current density of the first scan (LSV-1) was almost zero, and in the second scan (LSV-2), the current density can be observed but was still lower than  $0.3 \text{ mA cm}^{-2}$ . In the third scan (LSV-3), a more noticeable increase in the current density started at approximately  $1.1 \text{ V}$ . After the third scan, the mirror-like surface of the sample turned a matte color.



**Figure 1.** Linear sweep voltammetry curves (OCP- $2.4 \text{ V}$ ) of 316L stainless steel in a 2:1  $\text{AlCl}_3$ -EMIC ionic liquid with a scan rate of  $10 \text{ mV s}^{-1}$ . LSV-1, LSV-2 and LSV-3 represent the LSV curves of the first, second and third scans, respectively.

SEM images of the sample surface before and after LSV (OCP-2.4 V) are shown in Fig. 2. The original sample surface (Fig. 2a) was flat and without obvious pits and holes. After the first LSV measurement (Fig. 2b), pits with a diameter of approximately 1  $\mu\text{m}$  were observed. After the third LSV measurement (Fig. 2c), the diameter of the pits reached approximately 10  $\mu\text{m}$ . The morphology of the areas without pits in Fig. 2b and Fig. 2c remains the same as that of the original sample. The SEM results suggest that local dissolution occurred during the LSV measurement (OCP-2.4 V) process.



**Figure 2.** SEM images of the sample surface: (a) the original sample, (b) after the first LSV (OCP-2.4 V), and (c) after the third LSV (OCP-2.4 V).

Fig. 3 shows LSV curves of 316L stainless steel within the potential range from OCP to 5.0 V. In the first scan (LSV-1), an obvious anodic current started at 2.5 V, followed by two peaks. The maximum current density of the small peak (peak A) and the large peak (peak B) were approximately 1.0  $\text{mA cm}^{-2}$  and 10.2  $\text{mA cm}^{-2}$ , respectively. A yellow color appeared on the sample surface when the scanning potential exceeded 2.5 V and deepened as the polarization proceeded. The yellow color disappeared after stirring for 10 min, exposing a matte surface underneath. The second scan (LSV-2) was carried out next, and gray matter appeared on the sample surface during the process. The anodic current started at 1.0 V, and its density increased to 21.8  $\text{mA cm}^{-2}$  and then decreased rapidly to almost zero. The onset potential in the first scan was more positive than that in the second scan, which is an anodic behavior that also occurred for other metals [31, 32] and was explained as the strong inhibition of the oxide film for metal dissolution.

SEM images of the sample surface before and after LSV (OCP-5.0 V) are shown in Fig. 4. On the original sample surface (Fig. 4a), pre-existing polishing scratches can be clearly observed compared with Fig. 2a. After the first LSV measurement (OCP-5.0 V) (Fig. 4b), a uniform, velvet-like morphology

with grain boundaries (indicated by the arrow) was observed, which is completely different from the original morphology and the local dissolution morphology. This suggests that a general dissolution occurred during the LSV (OCP-5.0 V) process.

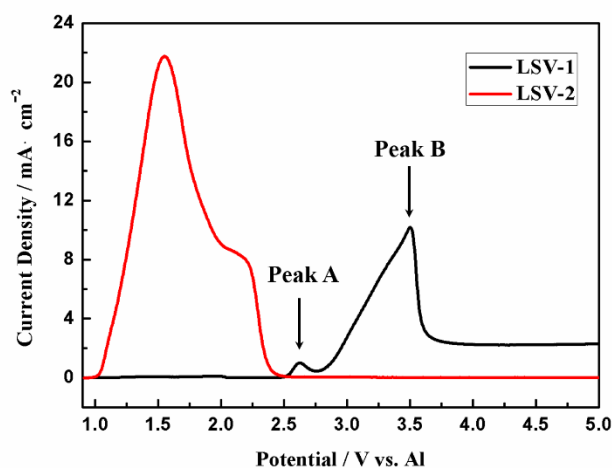


**Figure 3.** Linear sweep voltammetry curves (OCP-5.0 V) of 316L stainless steel in a 2:1  $\text{AlCl}_3$ -EMIC ionic liquid with a scan rate of  $10 \text{ mV s}^{-1}$ . LSV-1 and LSV-2 represent the LSV curves of the first and second scans, respectively.

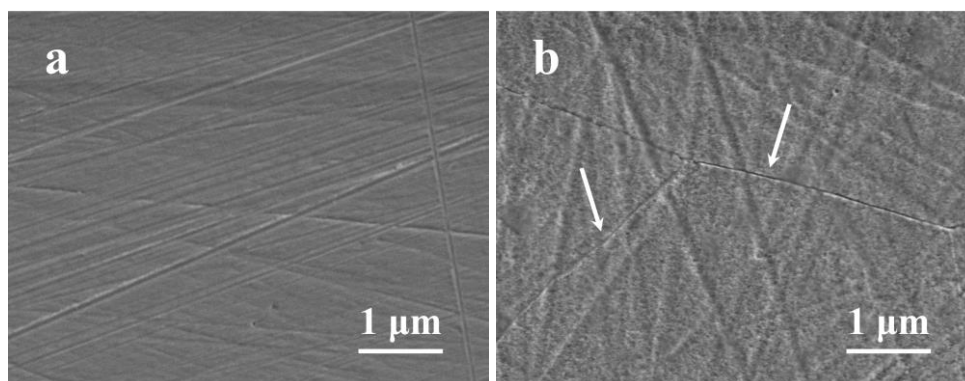


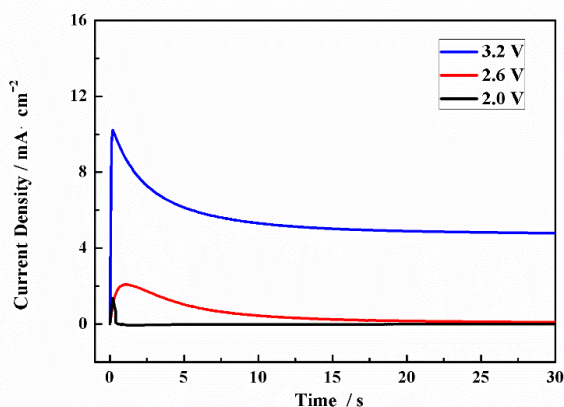
**Figure 4.** SEM images of the sample surface (a) before and (b) after LSV (OCP-5.0 V). The grain boundaries are indicated by the arrows.

As shown in the results above, both local and general dissolution of 316L stainless steel can occur in a 2:1  $\text{AlCl}_3$ -EMIC IL. The peak current density during the second LSV measurement was  $21.8$  and  $0.3 \text{ mA cm}^{-2}$  for LSV (OCP-5.0 V) and LSV (OCP-2.4 V), respectively, which implies that a much larger area of the oxide film was broken during the first LSV measurement (OCP-5.0 V). In addition, the surface morphology after general dissolution indicates that the oxide film was broken uniformly in a large number of locations. Based on the aforementioned characteristics, we referred to this breakdown of the oxide film as a general breakdown.

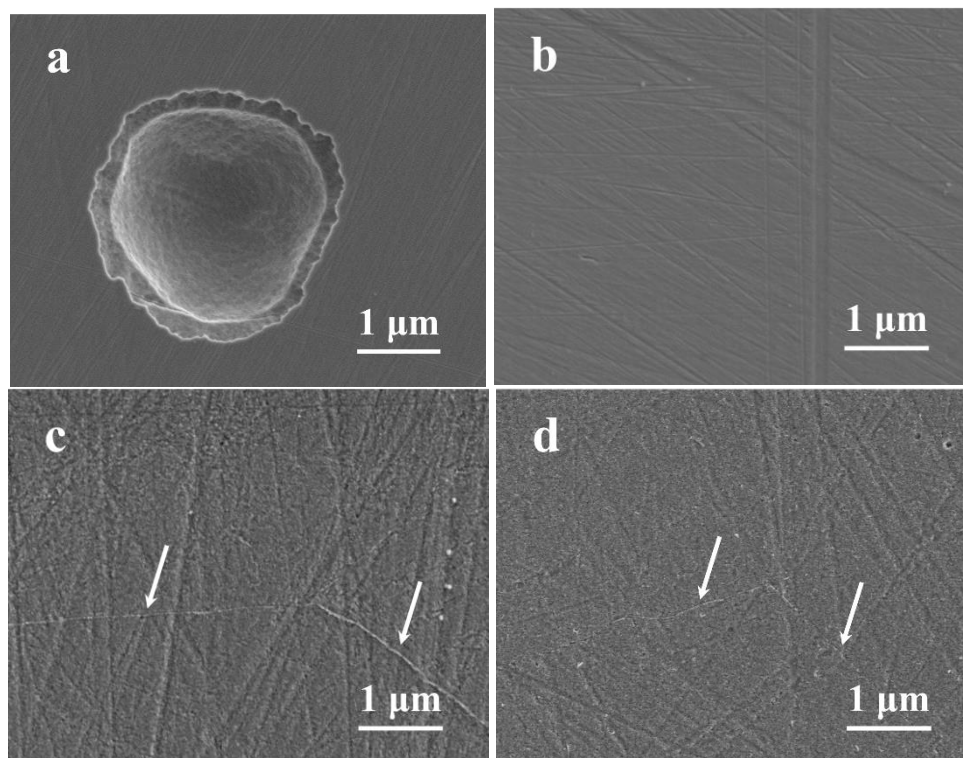
### 3.2. Chronoamperometry

To study the characteristics of the general breakdown of the oxide film, chronoamperometry was

carried out on the 316L stainless steel. Fig. 5 presents chronoamperometric curves at 2.0 V (before peak A), 2.6 V (peak A) and 3.2 V (peak B) vs. Al for 100 s, and only the results of the first 30 s are shown since the current density between 30 s - 100 s was unchanged. At the potential of 2.0 V (black line), the current density was almost zero except for the first 1 s, which suggests a negligible amount of metal dissolution. The mirror-like surface of the original sample remained unchanged after the experiment. At the potential of 2.6 V (red line) and 3.2 V (blue line); however, an obvious current can be observed. The current density increased instantaneously after a potential was applied, followed by a decrease until it reached a plateau. During the experiments at 2.6 V and 3.2 V, a yellow color appeared on the surfaces, and matte surfaces were observed after stirring during which the yellow color disappeared.



**Figure 5.** Chronoamperograms of 316L stainless steel in a 2:1 AlCl<sub>3</sub>-EMIC ionic liquid.

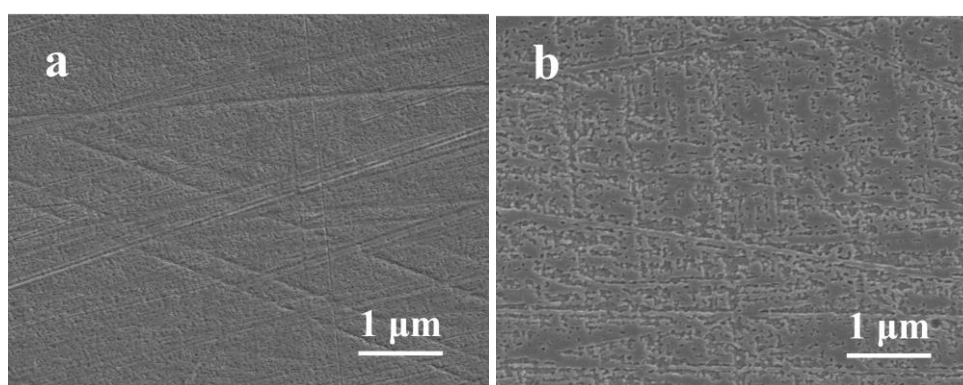


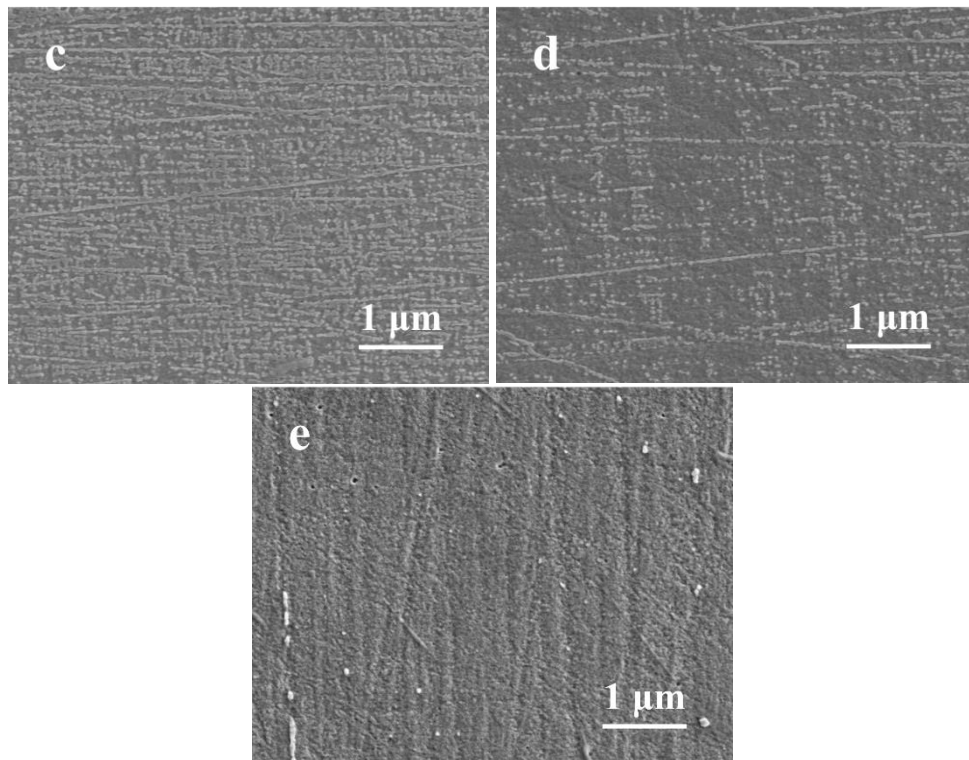
**Figure 6.** SEM images of the sample surface after chronoamperometry at (a)(b) 2.0 V, (c) 2.6 V, and (d) 3.2 V vs. Al for 100 s. The grain boundaries are indicated by the arrows.

Fig. 6 shows the micromorphology of the sample surface after chronoamperometry. Some pits can be observed on the surface after anodic dissolution at 2.0 V (Fig. 6a), while the other areas (Fig. 6b) remained the same as the original morphology in Fig. 4a. After anodic dissolution at 2.6 V (Fig. 6c) or 3.2 V (Fig. 6d), a uniform velvet-like morphology with grain boundaries was observed, indicating a general breakdown of the oxide film. Comparing the chronoamperometry results at three characteristic potentials (before peak A, at peak A, and at peak B), it can be concluded that the general breakdown occurred at a potential higher than the onset potential of peak A (2.5 V).

Fig. 7 shows the evolution of the surface morphology of the samples dissolved at 2.6 V vs. Al for different times. A large number of microholes were observed all over the surface after 1 s of dissolution (Fig. 7a). With increasing dissolution time, microholes expanded and interconnected, forming larger holes (Fig. 7b), and gradually developed into continuous dissolved areas (Fig. 7c). The undissolved areas of the surface decreased and formed 'isolated islands' (Fig. 7d). Eventually, most 'isolated islands' disappeared, and a uniform velvet-like appearance was observed (Fig. 7e). No obvious grain boundaries can be found in Fig. 7e, probably due to the dissolution time being shorter than that in Fig. 6c. The dissolution of a metal follows a planar pattern that is characterized as occurring parallel to the surface rather than vertically into the metal.

AFM was used to characterize the change in the surface morphology before and after a short dissolution time. It can be seen from Fig. 8a that the morphology of the original sample surface characterized by AFM is consistent with that by SEM (Fig. 4a). The microroughness  $R_a$  of the original sample was measured as 1 nm, lower than the macroroughness of 10 nm (as mentioned in Experimental Section) due to the measurement in a microscopic area. As shown in Fig. 8b, after dissolving at 2.6 V for 1 s, microholes can be observed clearly on the sample surface. The  $R_a$  was approximately 6 nm, higher than that of the original sample. As the thickness of the oxide film was approximately 3 nm, as described in the Experimental Section, it was concluded that the oxide film was indeed broken in a large number of positions in a short time.





**Figure 7.** SEM images showing the evolution of the surface appearance of the samples dissolved at 2.6 V vs. Al for (a) 1 s, (b) 2 s, (c) 5 s, (d) 10 s, and (e) 30 s.

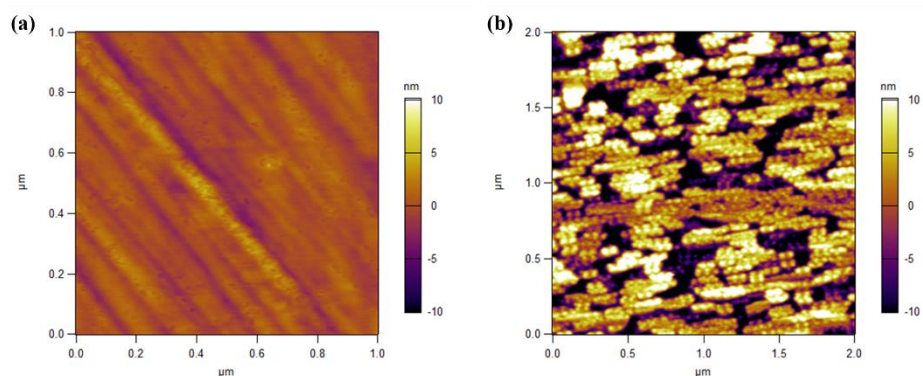


**Figure 8.** AFM images of (a) the original sample and (b) the sample dissolved at 2.6 V for 1 s.

### 3.3. Pulse potentiostatic method

In the previous linear sweep voltammetry and chronoamperometry experiments, the yellow color on the sample surface did not disappear for a few minutes after the current was turned off. It was speculated that the residual oxide film may have remained on the sample surface, which should have an effect on the subsequent processes. To understand the behavior of the oxide film after general breakdown, pulse potentiostatic experiments were carried out.

Fig. 9a shows the potential setup, where three pulses were applied in total on one sample. For each pulse, a potential pulse from 0 to 2.6 V vs. Al for 100 s was exerted. Fig. 9b shows the corresponding current density response, and only the results of the first 20 s are shown since the current density between

20 s - 100 s was basically unchanged. In the first pulse (red line), a small current density appeared and then slowly decreased to almost zero. After the first pulse, the sample surface showed a yellow color and remained unchanged as the sample remained immersed in the IL statically for 100 s. During the second pulse (blue line), which was conducted immediately thereafter, the current density was almost zero. After stirring for 10 min, the yellow color on the sample surface disappeared. In the third pulse (green line), the current density increased instantaneously to  $154 \text{ mA cm}^{-2}$ , far higher than that in the first pulse, and then decreased to almost zero. Gray matter was observed on the sample surface after the third pulse, similar to that during the second LSV scan (OCP-5.0 V), and it could dissolve into the IL after 100 s of static immersion.

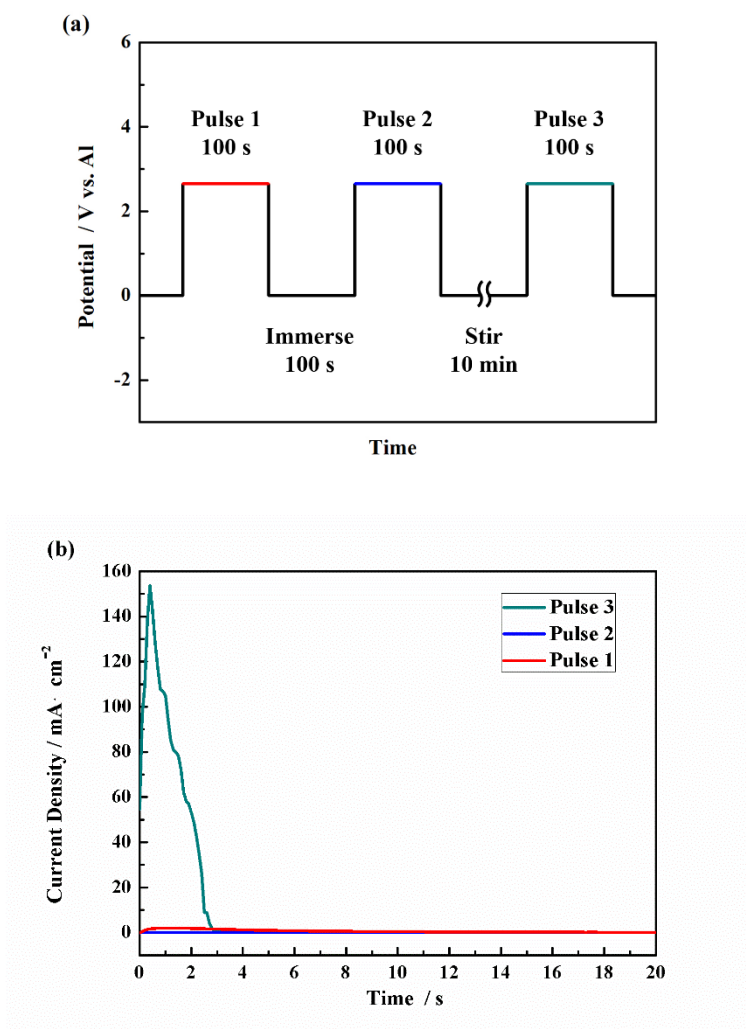


**Figure 9.** (a) The potential setup and (b) the current density during the different pulses of the pulse potentiostatic method.

The current density eventually decreased to zero for all three pulses, indicating that the sample was passivated by the dissolution product. The electric quantity required for passivation can be calculated according to the area under the curve in Fig. 9. In the first pulse, the calculated electric quantity was  $19 \text{ mC cm}^{-2}$ , which, based on Faraday's Law and the assumption that the dissolution product is Fe(II), is equivalent to a thickness of 7 nm of Fe. This implies that only a thin layer of the sample was dissolved before passivation. In contrast,  $218 \text{ mC cm}^{-2}$ , which is 11 times that of the original sample,

was required in the third pulse, indicating that a large quantity of dissolution occurred. In the second pulse, however, the electric quantity required was almost zero, which suggests that the sample was passivated at the start. The explanation for such a difference is given in the Discussion Section.

#### 4. DISCUSSION

The theories for the oxide film breakdown have been categorized into three main mechanisms that focus on the oxide film penetration, film breakdown, or adsorption [33, 34]. The penetration mechanism involves the transport of the anions through the oxide film to the metal-oxide interface. The film breakdown mechanism requires breaks (e.g., blistering, electrostriction stress and a cracking-healing mechanism) within the film that allow anions to reach the metal surface, enabling metal dissolution. The adsorption mechanism starts with the adsorption of aggressive anions on the oxide film surface, and aggressive anions form transient complexes with metal cations.

In Cl<sup>-</sup> containing aqueous solutions, local dissolution in the form of pitting occurred on 316L stainless steel when dissolving anodically [18-29]. The pitting potential is affected by several factors, such as the chloride ion concentration [21], surface roughness [22], microstructure [23], and ultraviolet irradiation [24]. The initial event during local dissolution is oxide film breakdown, in which corrosive species, especially Cl<sup>-</sup> ions, play an important role [25]. Okada et al. [26] considered the adsorption mechanism and proposed that local Cl<sup>-</sup> ions accumulated on the oxide film surface, formed metal chloride products and led to the breakdown of the oxide film. Macdonald et al. [27] considered the penetration mechanism and proposed that cation vacancies on the oxide film surface, generated by Cl<sup>-</sup> ions, migrated to the metal-film interface, and the accumulation of vacancies resulted in the breakdown of the oxide film. Recently, Saadi et al. [28] found that chloride ions existed at the interface of metal films using secondary ion mass spectrometry (SIMS) analysis. Combined with the phenomenon that the initiation of metastable pits was correlated to the cumulative charge density [29], they proposed that the local breakdown of 316L oxide film is consistent with the penetration mechanism; that is, Cl<sup>-</sup> ions penetrated the oxide film and accumulated at the interface of metal-film, leading to the breakdown of oxide film.

It can be seen from Results Section that there are two kinds of oxide film breakdown on 316L stainless steel in ionic liquids: local and general breakdown. General breakdown of the oxide film has the following characteristics. (1) It depends on the anodic potential and occurs only when the potential is higher than the onset potential of peak A (2.5 V). (2) It occurs instantaneously (less than 1 s) in a large number of positions throughout the surface. (3) It is followed by planar dissolution pattern as the anodic dissolution continues.

Considering the three oxide film breakdown mechanisms described above, the film breakdown mechanism could not explain the general breakdown because the number of breaks that this mechanism describes is limited. The adsorption mechanism can explain the complete removal of the oxide film but fails to explain the planar pattern of metal dissolution. The penetration mechanism can explain the experimental results of the general breakdown of the oxide film.

A large number of aggressive anions, such as chloride ions (Cl<sup>-</sup>), are critical in explaining the

general breakdown of the oxide film with the penetration mechanism. In an acidic 2:1 AlCl<sub>3</sub>-EMIC ionic liquid, the anodic limit of the electrochemical window is 2.5 V vs. Al [35], and the anodic reaction above the limit can be described as [35, 36]:



The onset potential of peak A (2.5 V) was close to the anodic limit, which suggests that peak A is related to reaction (1). However, no gas was observed on the oxide surface during the experiments; thus, it was speculated that there exists a series of stepwise reactions illustrated in reactions (2)-(4) [37] or reactions (5)-(7) [38]:



As a consequence of either series of reactions, Cl<sup>-</sup> are generated and adsorb on the oxide surface when the potential is higher than 2.5 V, which explains the potential dependence of the general breakdown. The yellow color that was observed may be due to the generation and absorption of Cl<sub>3</sub><sup>-</sup> [38, 39] on the oxide film. In a strong electric field, Cl<sup>-</sup> penetrates the oxide film and reaches the interface of the metal and the oxide film. The penetration process is autocatalytic because the incorporation of anions contaminates the film and leads to higher ionic conductivities along the penetration paths [33], thus causing the oxide film to break instantaneously. The penetration probably occurs at the position of oxygen vacancies in the oxide film [40], causing breakdown in many positions throughout the surface uniformly (Fig. 10a), which is, according to our description in the Results Section, a general breakdown.



At the interface, the oxidation reaction (8) occurs, generating metal chloride salts between the metal and the oxide film. Usually, the salts occupy two to eight times the volume of the metal or the oxide film [41]. Due to the expansive force, the oxide film on the surface is broken, and microcracks between the metal and the oxide film are formed around the salts (Fig. 10b). The IL flows through the microcracks, and when it reaches the bare metal, salts are formed from the electrochemical dissolution of the metal and lead to a passivating film [42]. The volume expansion of the salts generates more microcracks and further separates the metal and the oxide film. The alternate reaction of salt generation and microcrack formation leads to the planar pattern of metal dissolution (Fig. 10c). In addition, metal chloride salts generated through reaction (8) may remain on the surface and contribute to the passivation of the metal; they may also dissolve in the IL that flows through the microcracks and thus expose the bare metal to the IL, which leads to anodic dissolution and eventual passivation.

The aforementioned process occurred during the first pulse of the pulse potentiostatic experiments, and as the dissolution only took place on the interface of the metal and the oxide film, the amount of electric required to passivate it was small. During the subsequent static immersion, the broken oxide film remained on the surface, as indicated by the yellow color, thus inhibiting the salts from dissolving. As a result, during the second pulse, the surface remained passivated. The salts and the broken oxide film were removed during the subsequent stirring process, so an 11-fold multiplication in electric

quantity was observed during the third pulse as the bare metal was subject to anodic dissolution.

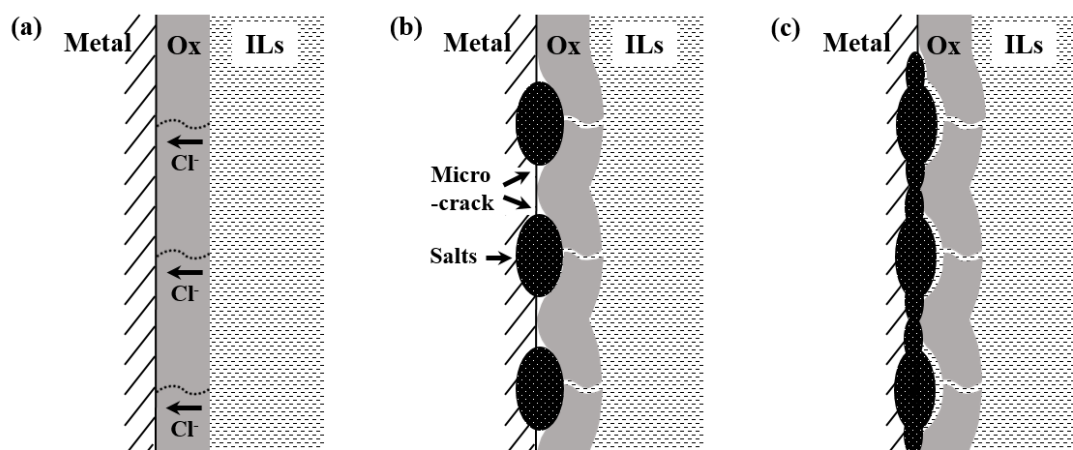


**Figure 10.** Schematic diagrams of the general breakdown of the oxide film: (a) penetration of  $\text{Cl}^-$ , (b) breakdown of oxide film, and (c) planar dissolution pattern.

A small amount of  $\text{Cl}^-$  ions existed in the acidic 2:1  $\text{AlCl}_3$ -EMIC ionic liquid, based on the equilibrium reaction (2). When the potential was more negative than the anodic limit of the electrochemical window (2.5 V), the local breakdown of oxide film occurred, which may be due to the penetration of a small amount of  $\text{Cl}^-$  ion through the film or defects in the oxide film. The mechanism requires further study.

## 5. CONCLUSIONS

The breakdown of the oxide film on 316L stainless steel in a 2:1  $\text{AlCl}_3$ -EMIC ionic liquid was studied in this paper. The results showed that the general breakdown depended on the potential and occurred when it was higher than 2.5 V. The general breakdown occurred instantaneously (less than 1 s) and was followed by a planar dissolution pattern, and the broken oxide film remained on the surface unless it was removed during stirring. The breakdown can be explained by  $\text{Cl}^-$  penetrating the oxide film.

## References

1. F. J. Monteiro, M. A. Barbosa, D. H. Ross, and D. R. Gabe, *Surf. Interface Anal.*, 17 (1991) 519.
2. J. E. Gray and B. Luan, *J. Alloys Compd.*, 336 (2002) 88.
3. C.-O. A. Olsson and D. Landolt, *Electrochim. Acta*, 48 (2003) 1093.
4. Q. X. Liu, S. Z. E. Abedin, and F. Endres, *Surf. Coat. Technol.*, 201 (2006) 1352.
5. B. J. Xu, J. Chen, and G. P. Ling, *Electrochem. Solid-State Lett.*, 15 (2012) D1.
6. B. J. Xu, M. Zhang, and G. P. Ling, *Surface & Coatings Technology*, 239 (2014) 1.
7. F. Endres, D. MacFarlane, and A. Abbott, *Electrodeposition from Ionic Liquids*, Wiley (2008), Weinheim, Germany.
8. A. P. Abbott, G. Frisch, and K. S. Ryder, *Annu. Rev. Mater. Res.*, 43 (2013) 335.
9. B. J. Xu, R. Qu, and G. P. Ling, *Electrochim. Acta*, 149 (2014) 300.
10. R. Qu, Y. D. Jiang, B. J. Xu, J. J. Ding, C. Liao, and G. P. Ling, *J. Rare Earths*, 33 (2015) 776.
11. Q. B. Zhang, Y. X. Hua, and Z. R. Zhou, *Int. J. Electrochem. Sci.*, 8 (2013) 10239.

12. Y. C. Wang, T. C. Lee, J. Y. Lin, J. K. Chang, and C. M. Tseng, *Corros. Sci.*, 78 (2014) 81.
13. P. C. Lin, I. W. Sun, J. K. Chang, C. J. Su, and J. C. Lin, *Corros. Sci.*, 53 (2011) 4318.
14. A. P. Abbott, G. Capper, K. J. Mckenzie, and K. S. Ryder, *Electrochim. Acta*, 51 (2006) 4420.
15. Y. D. Jiang, L. Z. Luo, S. F. Wang, R. Bin, G. K. Zhang, and X. L. Wang, *Appl. Surf. Sci.*, 427 (2018) E70.
16. Y. D. Jiang, L. Z. Luo, J. Mei, and X. L. Wang, *J. Rare Earths*, 36 (2018) 1221.
17. D. P. Xue, Y. M. Chen, G. P. Ling, K. Z. Liu, C. A. Chen, and G. K. Zhang, *Fusion Engineering and Design*, 101 (2015) 128.
18. P. M. Natishan, *Corrosion*, 74 (2018) 263.
19. X. Wu, Y. Sun, Y. Liu, Y. Yang, J. Li, and Y. Jiang, *J. Electrochem. Soc.*, 165 (2018).
20. C. Mana, C. Donga, T. Liu, D. Kong, D. Wang, and X. Li, *Appl. Surf. Sci.*, 467-468 (2019).
21. Y. Tang, Y. Zuo, J. Wang, X. Zhao, B. Niu, and B. Lin, *Corros. Sci.*, 80 (2014).
22. A. Shahryari, W. Kamal, and S. Omanovic, *Mater. Lett.*, 62 (2008).
23. S. Tanhaei and K. Gheisari, *Int. J. Min. Met. Mater.*, 25 (2018).
24. C. B. Breslin, D. D. Macdonald, E. Sikora, and J. Sikora, *Electrochim. Acta*, 42 (1997).
25. A. Pardo, M. C. Merino, A. E. Coy, F. Viejo, R. Arrabal, and E. Matykin, *Corros. Sci.*, 50 (2008).
26. T. Okada, *Corros. Sci.*, 31 (1990).
27. S. F. Yang and D. D. Macdonald, *Electrochim. Acta*, 52 (2007).
28. S. A. Saadi, Y. Yi, P. Cho, C. Jang, and P. Beeley, *Corros. Sci.*, 111 (2016).
29. M. A. Ameri, Y. Yi, P. Cho, S. A. Saadi, C. Jang, and P. Beeley, *Corros. Sci.*, 92 (2015).
30. J. S. Wilkes, J. A. Levisky, R. A. Wilson, and C. L. Hussey, *Inorganic Chemistry*, 21 (1982) 1263.
31. P. R. Gonzalez and G. P. Ling, *Surf. Coat. Technol.*, 331 (2017) 57.
32. A. P. Abbott, G. Capper, K. J. McKenzie, A. Glidle, and K. S. Ryder, *Phys. Chem. Chem. Phys.*, 8 (2006) 4214.
33. J. Soltis, *Corros. Sci.*, 90 (2015) 5.
34. G. S. Frankel, *J. Electrochem. Soc.*, 145 (1998) 2186.
35. C. Scordilis-Kelley, J. Fuller, R. T. Carlin, and J. S. Wilkes, *J. Electrochem. Soc.*, 139 694.
36. T. J. Melton, J. Joyce, J. T. Maloy, J. A. Boon, and J. S. Wilkes, *J. Electrochem. Soc.*, 137 (1990) 3856.
37. C. Villagran, C. E. Banks, C. Hardacre, and R. G. Compton, *Anal. Chem.*, 76 (2004) 1998.
38. X. H. Li, A. Van den Bossche, T. Vander Hoogerstraete, and K. Binnemans, *Chem. Commun.*, 54 (2018) 475.
39. K. Haerens, E. Matthijs, K. Binnemans, and B. V. d. Bruggen, *Green Chem.*, 11 (2009) 1357.
40. E. McCafferty, *Corros. Sci.*, 45 (2003) 1424.
41. G. T. Burstein, P. C. Pistorius, and S. P. Mattin, *Corros. Sci.*, 35 (1993) 57.
42. D. P. Xue, Y. Yang, and G. P. Ling, *Green Energy & Environment*, 2 (2017) 412.